RSC Advances

PAPER

View Article Online
View Journal | View Issue

Cite this: *RSC Adv.*, 2014, **4**, 20262

Co-template method provides hierarchical mesoporous silicas with exceptionally ultra-low refractive indices†

Chu-Chian Liu, Jheng-Guang Li and Shiao-Wei Kuo*

Received 18th February 2014
Accepted 16th April 2014

DOI: 10.1039/c4ra01392a

www.rsc.org/advances

In this study we prepared hierarchical mesoporous silicas through evaporation-induced self-assembly using the triblock copolymer poly(ethylene oxide-*b*-propylene oxide-*b*-ethylene oxide) (F127) and the diblock copolymer poly(ethylene oxide-*b*-ε-caprolactone) (PEO-*b*-PCL) as co-templates. Small-angle X-ray scattering, transmission electron microscopy, and scanning electron microscopy revealed that these hierarchical mesoporous structures were greatly affected by the volume fraction of each component segment in the block copolymers of this co-template system. Furthermore, N_2 isotherm sorption analyses of our unique hierarchical mesoporous structures indicated that their BET surface areas reached as high as 781 $m^2\ g^{-1}$, with pore volumes as high as 0.99 $cm^3\ g^{-1}$; they possessed a structure of regular spherical strip arrangements alternating with tetragonal cylinders. Using an n&k analyzer and a spin-coating method, we found that the samples displayed ultra-low refractive indices (*ca.* 1.08), suggesting that such hierarchical mesoporous silicas have potential for application in various fields (*e.g.*, as anti-reflectance films for solar cells).

Introduction

Mesoporous materials ordered hierarchically on multiple length scales are attracting considerable attention for both their theoretical qualities and their practical applications.[1] These materials can possess outstanding physicochemical properties, including high surface areas, large pore volumes, a variety of pore structures, and mechanical stability, giving them broad potential applications in, for example, adsorption,[2] separation,[3] catalysis,[4] drug delivery,[5] and antireflective surfaces.[6] Several hierarchical self-assembled nanostructures have been reported in recent years.[7] For example, ABC-type triblock copolymers have been attractive materials in recent years because they can self-assemble into various structures, including three-phase lamellae, core/shell cylinders, and other hierarchical structures.[7a]

In previous studies,[8] we used a simple ABC-type triblock copolymer, poly(ethylene-*b*-ethylene oxide-*b*-caprolactone) (PE-*b*-PEO-*b*-PCL), as a single template for the fabrication of hierarchical mesoporous silicas through evaporation-induced self-assembly (EISA). Using this approach, we obtained two particularly well-ordered hierarchical structures, namely "alternate body-centered cubic" and "tetragonal cylinder alternated with face-centered cubic." The "tetragonal cylinder alternated with face-centered cubic" structure possessed two differently sized mesopores: small spherical mesopores (*ca.* 3.8 nm) and large cylindrical mesopores (*ca.* 8.6 nm) resulting from the PE and PCL segments, respectively. That study was the first to employ an amphiphilic ABC-type triblock copolymer as a single template for the fabrication of hierarchical mesoporous silicas; nevertheless, the synthesis of triblock copolymers can be a difficult and time-consuming means of varying the volume fractions of block copolymer segments.[9] In contrast, the use of co-templates, by blending two kinds of diblock copolymers (*e.g.*, AB and BC diblock copolymers) is a relatively simpler method for changing the volume fraction of each component polymer.[9,10] The key point when using a co-template approach to prepare hierarchical self-assembled structures is to ensure similar molecular weights of the B blocks in the AB/BC diblock copolymer mixtures.[9–11]

Mesoporous materials exhibiting interesting surface topologies can also be applied as optical materials because of their transparency (feature scales less than the wavelength of the incoming light) and low refractive indices, which depend on the degree of porosity and the refractive indices of the nonporous parts. Their low refractive indices (low-*n*) suggest that we can enhance performance in many photonics applications, such as broad band antireflection coatings with air ambient,[12,13] surface plasmon-coupled emission (SPCE) and Tamm state-coupled emission (TSCE),[14] omnidirectional reflectors,[15,16] distributed Bragg reflectors DBRs,[17] multilayer complex photonic structures able to localize the electromagnetic field.[18] Several rules must be

Department of Materials and Optoelectronic Science, Center for Nanoscience and Nanotechnology, National Sun Yat-Sen University, Kaohsiung, 804, Taiwan. E-mail: kuosw@faculty.nsysu.edu.tw

† Electronic supplementary information (ESI) available. See DOI: 10.1039/c4ra01392a

obeyed in to the quest to eliminate reflection at the interface between the atmosphere and an anti-reflection structure. First, n_c should be less than or equal to $(n_s n_o)^{1/2}$, where n_c, n_s, and n_o are the refractive indices of the anti-reflection structure, the substrate, and air, respectively.[19] Second, the thickness of the anti-reflection thin film must be one quarter of the wavelength of the incident light. For glass and most plastics, the value of n_s is approximately 1.5, so the value of n_c must be less than 1.22. This required value of n_c is so low that no known bulk materials can meet this criterion. Decades of research have provided an abundance of papers describing the use of multiple-layering methods to fabricate materials exhibiting low refractive indices.[20–26] From the considerations of fabrication time, manpower, and cost, however, it would be better to develop single-layer coatings. Nevertheless, the lowest refractive index of a dense material (MgF_2) is approximately 1.35; thus, a single layer cannot naturally have a refractive index lower than this value. Accordingly, many approaches have been developed—including electron-beam writing,[20] selective dissolution,[21] lithography techniques,[23] nanoparticle multilayers,[23,24] and alignment of liquid crystals[26,27]—to create coatings with very low refractive indices, although their resulting mechanical properties are generally poor. The practical applications of these materials have, therefore, been limited because of the poor heat resistance of the substrates and the complexity of the fabrication processes.

In this study, we employed a co-template method to fabricate hierarchical mesoporous silicas, using the diblock copolymer poly(ethylene oxide-*b*-caprolactone) (PEO_{114}-*b*-PCL_{88}; to provide larger mesopores) and the commercial triblock copolymer poly(ethylene oxide-*b*-propylene oxide-*b*-ethylene oxide) (PEO_{106}-*b*-PPO_{70}-*b*-PEO_{106}, F127; to provide smaller mesopores) as co-templates at various weight ratios with respect to tetraethyl orthosilicate (TEOS, as the matrix). Here, the molecular weights of the PEO block segments in the diblock copolymer PEO-*b*-PCL and the triblock copolymer F127 were very similar (degrees of polymerization of the PEO segments in the PEO-*b*-PCL and F127 block copolymers were 114 and 106, respectively). The combination of this simple co-template method and an EISA strategy allowed us to fabricate a series of hierarchical mesoporous silica materials, including "regular spherical strip arrangement alternated with tetragonal cylinder" and "random small sphere alternated with large sphere" structures. Thin films of these hierarchical mesoporous silicas, formed using spin coating method, displayed BET surface areas as high as 781 $m^2\ g^{-1}$, pore volumes as high as 0.99 $cm^3\ g^{-1}$, and refractive indices as low as 1.08.

Experimental section

Materials

The triblock copolymer Pluronic F127 was obtained from Aldrich. Monomethoxy-poly(ethylene glycol) having a molecular weight of 5000 (MPEG-5K) was obtained from Fluka and dried through azeotropic distillation with toluene. ε-Caprolactone (ε-CL, Acros) was purified through vacuum distillation over CaH_2; the distillation fraction collected at 96–98 °C (5 mmHg) was used in all polymerization reactions. Stannous(II)octoate [$Sn(Oct)_2$, Sigma] was used as received. Methylene chloride was dried over CaH_2 prior to use. The diblock copolymer PEO_{114}-*b*-PCL_{88} was prepared through the ring-opening polymerization of ε-CL in the presence of mPEG-5K, with $Sn(Oct)_2$ as the catalyst.[28] Hexane, tetrahydrofuran (THF), and TEOS were used as received. Deionized water was used in all experiments.

Hierarchical mesoporous silicas

Hierarchical mesoporous silicas were prepared through an EISA strategy in THF, using the block copolymers PEO-*b*-PCL and F127 as co-templates and TEOS as the silica precursor. In a typical synthetic procedure, TEOS (0.1 g) and 0.1 M HCl (0.1 g) were added to a THF solution (5 g) of the diblock copolymer PEO-*b*-PCL and the triblock copolymer F127 (2.0 wt%) and then the mixture was stirred for 30 min. The resulting homogeneous solution was poured into Petri dishes, which were left at room temperature for 48 h to evaporate the THF. The transparent films were collected and ground into powders. The powders were transferred into a PFA bottle containing 1.0 M HCl (30 mL) and treated hydrothermally at 100 °C for 3 days. The product was washed with water and EtOH, dried at room temperature, and calcined in air at 600 °C (in a furnace at a heating rate of 1 °C min^{-1}) to produce a white mesoporous silica (Scheme 1).

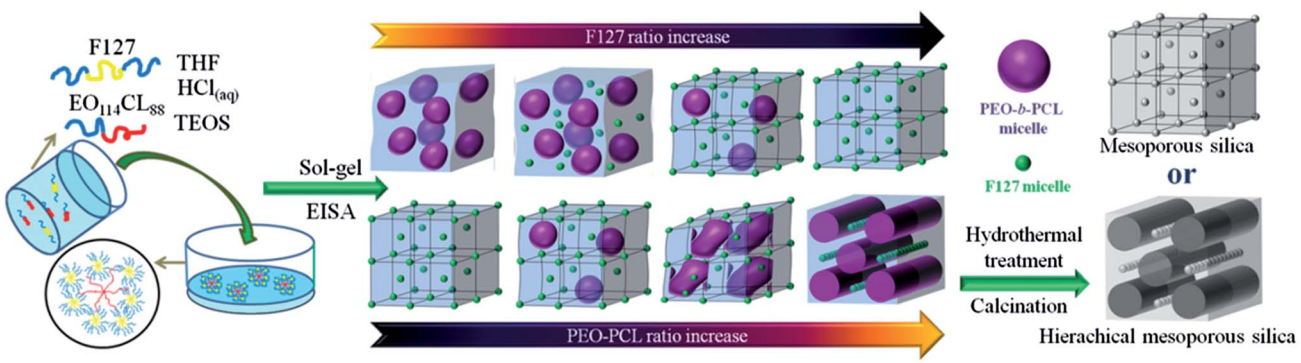

Scheme 1 Fabrication of mesoporous silica with specific hierarchical mesostructure.

Low-*n* thin films of hierarchical mesoporous silicas

Specific amounts of the diblock copolymer PEO-*b*-PCL and the triblock copolymer F127 were dissolved in THF (5 g). Prior to coating, 0.1 M HCl (0.10 g) was added to the bottle and then the mixture stirred for 30 min. The resulting homogeneous solution was spin-coated (1500 rpm, 80 s) onto glass and then the film was calcined in air at 600 °C for 6 h to form a low-*n* thin film of hierarchical mesoporous silicas (Scheme 2).

Characterization

Small-angle X-ray scattering (SAXS) was performed using a NANOSTAR U small-angle X-ray scattering system (Bruker AXS Gmbh, Karlsruhe, Germany) and Cu Kα radiation (30 W, 50 kV, 600 μA). The d spacings were calculated using the formula $d = 2\pi/q$, where q is the scattering vector. Transmission electron microscopy (TEM) images were recorded using a JEOL 3010 microscope operated at 200 kV; samples for TEM measurements were suspended in EtOH and supported onto a holey carbon film on a Cu grid. Nitrogen adsorption/desorption isotherms were measured at 77 K using an ASAP 2020 analyzer; prior to measurement, the samples were degassed under vacuum at 200 °C for at least 6 h. The Brunauer–Emmett–Teller (BET) method was employed to calculate the specific surface areas. Using the Broekoff–de Boer (BdB) sphere model, the pore volumes and pore size distributions were derived from the adsorption branches of the isotherms; the total pore volumes were estimated from the amount adsorbed at a relative pressure (P/P_0) of 0.995. The calibration curve was obtained using silica–alumina (part no. 004-16821-00) as a reference material and N_2 as the adsorption gas. High-resolution scanning electron microscopy (HRSEM) images were recorded using a field emission JEOL.

JSM-6700F (Japan) instrument operated at 30 kV. The film thicknesses and refractive indices of the hierarchical mesoporous materials were measured using an n&k Analyzer 1280 (n&k Technology) at wavelengths ranging from 190 to 1000 nm.

The n&k Analyzer is a type of thin film measurement system based on the patented "n&k method". The system consists of proprietary software for the thin film analysis, a spectrophotometer to measure reflectance, an x–y stage, a personal computer. With the n&k Analyzer, thickness (d), index of refraction (n), extinction coefficient (k), energy bandgap (E_g), interface roughness (σ) can be determined for semiconductors, transparent conductors, photoresists, polymers, color filters and very thin metal films. The measurement technique is based on the well established "n&k method". This methods utilizes the Forouhi–Bloomer[29–31] dispersion equations and the broad band (1900–10 000 A) reflectance spectrum. Forouhi–Bloomer deduced a physical model for refractive index n and extinction coefficient k in terms of λ and materials parameters, applicable to a wide range of semiconductor and dielectric films. The Forouhi–Bloomer model is valid over the deep ultraviolet – near infrared wavelength range. The Forouhi–Bloomer equation fit experimental data over this very wide wavelength range and they require few parameters as shown below:

$$k(E) = \sum_{i=1}^{q} \frac{A_i(E - E_g)^2}{E^2 + B_i E + C_i}$$

$$n(E) = n(\infty) + \sum_{i=1}^{q} \frac{B_{0i}E + C_{0i}}{E^2 + B_i E + C_i}$$

In these equations E is the photo energy related to the wavelength of light according to $E = hc/\lambda$, where h is Planck's constant and c is speed of light in vacuum. E_g is energy band

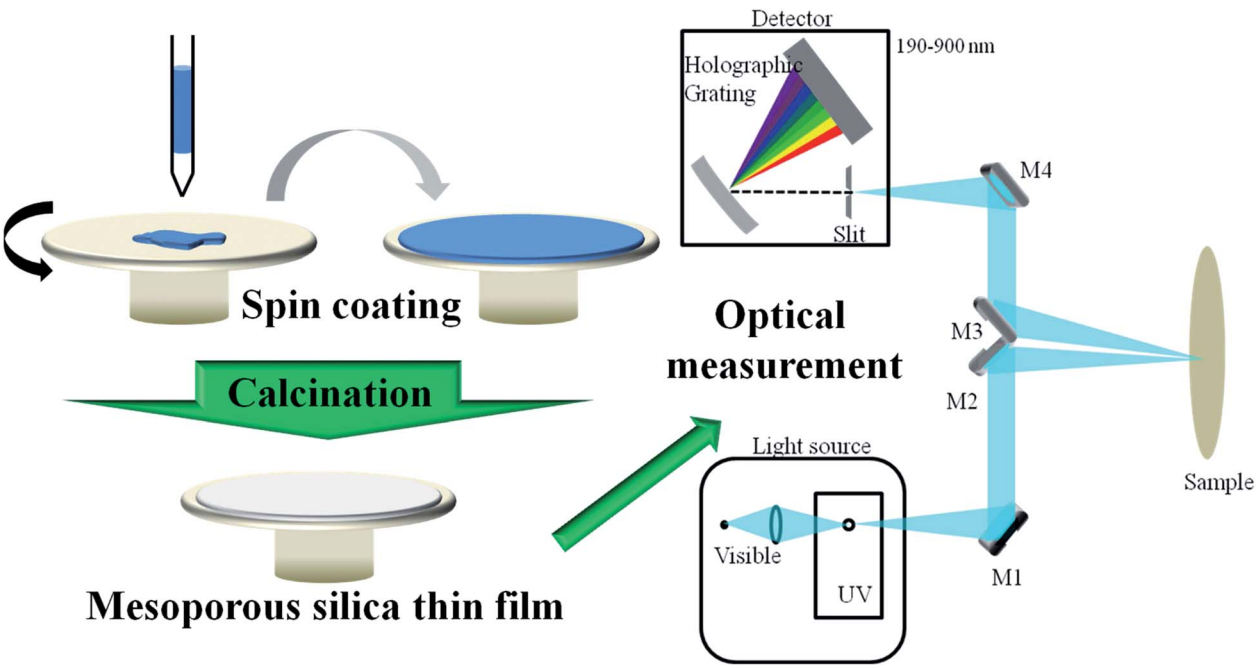

Scheme 2 Preparation of hierarchical mesoporous silica thin films and the refractive index measurement.

gap, and A, B, and C are not mere fitting parameters, but are related to electronic structure of the material. The quantities B_0 and C_0 are not independent parameters, but depend on A, B, C, and E_g.

Results and discussion

Mesoporous silicas prepared at various F127-to-PEO–PCL ratios under fixed TEOS-to-co-template weight ratios

To understand the phase behavior of the hierarchical mesoporous silicas, we used TEM, SAXS, and BET analyses to identify and characterize a series of mesoporous silicas prepared by changing the weight ratios between F127 and PEO-*b*-PCL at a fixed weight ratio of TEOS to the co-template (3 : 1). Fig. 1(b) displays SAXS data obtained upon changing the weight ratio of F127 to PEO-*b*-PCL (*e.g.*, F30EL70 represents the sample obtained when the F127-to-PEO-*b*-PCL weight ratio was 30 : 70). The first peak at a value of q of 0.308 nm^{-1} (d = 20.38 nm) represents pure PEO-*b*-PCL as a single template; the second weaker-order peak at $3^{1/2}q^*$ indicates a cylinder mesostructure, as revealed in the TEM image in Fig. 1(a)-(i).[21] In addition, the first peak belonging to pure F127 as a single template appears at a value of q of 0.579 nm^{-1} (d = 10.84 nm); the SAXS pattern of the bcc-type mesoporous structure featured a peak ratio of $1 : 3^{1/2} : 4^{1/2} : 5^{1/2}$ indexed as having (110), (211), and (220) reflections, corresponding to a cubic structure, as confirmed by the TEM image in Fig. 1(a)-(viii) {$Im\bar{3}m$ space group; also confirmed by TEM images with different orientations ([100],

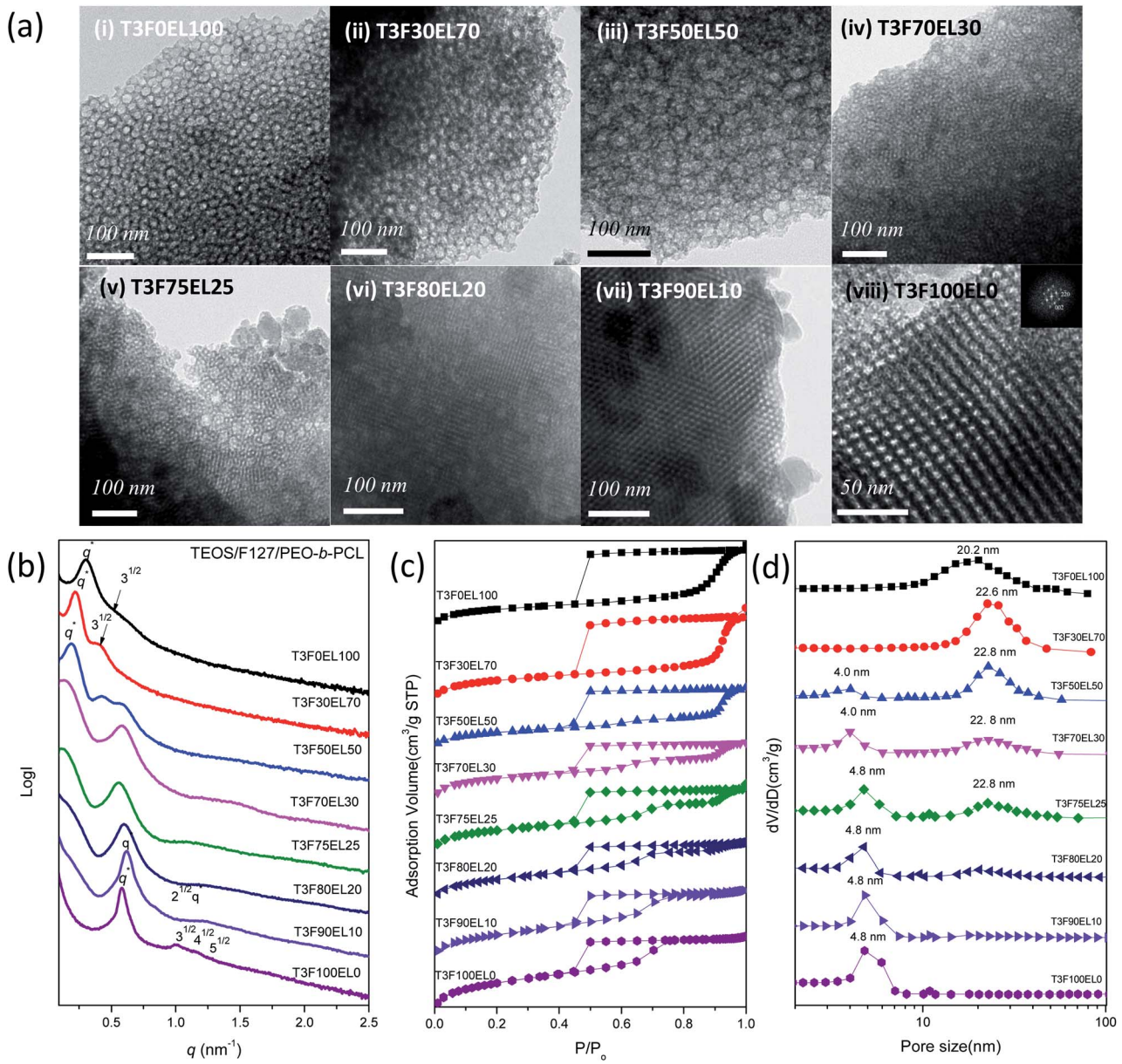

Fig. 1 (a) TEM images, (b) SAXS patterns, (c) N_2 adsorption–desorption isotherms, and (d) pore size distribution curves of hierarchical mesoporous silicas prepared at a fixed TEOS-to-co-template ratio (3 : 1) and various F127-to-PEO-*b*-PCL ratios.

[110], and [111] planes, as displayed in Fig. S1†)}. The first peak from the PEO-*b*-PCL template shifted significantly to the lower-q region upon increasing the F127 content (*e.g.*, at 30 wt%: $q_{max} = 0.218$ nm^{-1}; d-spacing = 28.8 nm; at 50 wt%: $q_{max} = 0.186$ nm^{-1}; d-spacing = 33.7 nm; at 70 wt%: $q_{max} = 0.151$ nm^{-1}; d-spacing = 41.5 nm; at 75 wt%: $q_{max} = 0.116$ nm^{-1}; d-spacing = 54.1 nm), indicating an increase in the d-spacing. The first peak become broad, however, and the second peak disappeared when the F127 content was greater than 70 wt%, indicating the short range order of a spherical micelle mesostructure. For the mesoporous silica sample prepared at 30 wt% F127, we observed only relative large pores (*ca.* 20 nm) from the TEM image [Fig. 1(a)-(ii)]. When the F127 content was 50 wt%, we observed clear scattering peaks for both PEO-*b*-PCL and F127; the corresponding TEM image revealed the first type of hierarchical mesostructure—random small spheres alternated with large spheres [Fig. 1(a)-(iii)]. Further increasing the F127 content to 70, 75, and 80 wt% resulted in similar hierarchical mesostructures; the d-spacing of the small spheres did not change significantly, but the inter-spherical micelle distance did increase upon increasing the F127 content, as indicated in Fig. 1(a)-(iv) to 1(a)-(vi). These mesostructures gradually transformed into long-range-ordered BCC structures when the F127 contents reached 90 and 100 wt%. The scattering profiles of these blends included the reflection peaks of the pure block copolymer, indicating that macro-phase separation had occurred in the PPO/PCL blends.[32,33]

Fig. 1(c) presents the N_2 sorption curves for all mesoporous silicas; their representative type-IV curves with capillary condensation steps in the relative pressure range from 0.45 to 0.95 exhibited H_2-like hysteresis loops, characteristic of cage-like mesopores. Samples having F127 contents from 50 to 80 wt % (*i.e.*, T3F50EL50 to T3F80EL20) provided two hysteresis loops in one curve, with the first, from 0.45 to 0.75, contributed by F127 and the other, from 0.45 to 0.95, contributed by PEO-*b*-PCL. These patterns also suggest the presence of spherical mesopores of two different sizes. Based on the BdB model [Fig. 1(d)], these mesoporous silica samples possess bimodal characteristics: a combination of smaller spherical mesopores (4–5 nm) and larger spherical mesopores (20–23 nm). The smaller ones resulted from the presence of F127; the larger ones arose from PEO-*b*-PCL. Finally, we observed pores having a diameter of only approximately 5 nm when the F127 weight ratio reached to 90–100 wt%. Table 1 summarizes the BET surface areas, pore volumes, and pore sizes of these mesoporous silica materials; the micropore surface area and micropore volume increased dramatically upon increasing the content of F127 to 70 wt%, but they decreased at 75 wt%. Fig. 2(a) and (e) summarize a possible mechanism for the phenomenon of obtaining cylindrical pores with short-range order when using pure PEO-*b*-PCL as a single template. The small spherical pores appeared upon increasing the F127 content; we did not, however, observe such small spherical pores at relative low F127 contents (<50 wt%) in the TEM images and BET pore size distribution plot, presumably because the hydrophilic PPO segments also interacted strongly with the silica matrix at relatively high TEOS/PPO ratios and, thus, most of the F127 block copolymers were located in the silica matrix. Further increasing the F127 content to 50 and 70 wt% caused the F127 to phase-separate from the silica matrix and form its own domains, subsequently resulting in observable smaller spherical mesopores (4 nm). Because of their similar contents of smaller and larger spherical mesopores, the highest micropore surface area and micropore volume occurred when the F127 content was 70 wt% [Fig. 2(b) and (f)]. In addition, when the F127 content was greater than 75 wt%, the phase-separation of F127 from the silica matrix was complete and, thus, the diameter of the spherical mesopores increased to 4.8 nm, equal to that obtained when using pure F127 as a single template [Fig. 2(d) and (h)]. The inter-distance between the larger spherical mesopores templated by PEO-*b*-PCL increased upon increasing the F127 contents [*e.g.*, Fig. 2(c) and (g)], based on the SAXS data in Fig. 1(b), because of phase-separation of F127 from the silica matrix.

Mesoporous silicas prepared at a fixed TEOS-to-F127 ratio and various contents of PEO-*b*-PCL

For this study, we observed the morphological transitions that occurred upon changing only the content of PEO-*b*-PCL to control the volume fraction. Here, we employed two TEOS-to-F127 ratios (3 : 0.75 and 3 : 0.9) and changed the PEO-*b*-PCL weight ratios to fabricate a series of hierarchical mesoporous silica samples. Fig. 3(a) and (b) display TEM images and SAXS patterns, respectively, of hierarchical mesoporous silica samples prepared at a fixed TEOS-to-F127 ratio of 3 : 0.75 with various PEO-*b*-PCL contents. The TEM images of samples T3F75EL25 to T3F75EL100 all reveal the same structure:

Table 1 Textural properties of mesoporous silica samples templated by F127 and PEO-*b*-PCL at fixed TEOS-to-template ratios

Sample	Pore size (nm)	S_{BET} (m^2 g^{-1})	S_M (m^2 g^{-1})	Pore volume (cm^3 g^{-1})	Micropore volume (cm^3 g^{-1})
T3EL100	20.2	573	227	0.74	0.101
T3F30EL70	22.6	628	203	0.83	0.089
T3F50EL50	4.0; 22.8	522	193	0.57	0.086
T3F70EL30	4.0; 22.8	671	252	0.57	0.112
T3F75EL25	4.8; 22.8	624	175	0.63	0.076
T3F80EL20	4.8	642	148	0.56	0.063
T3F90EL10	4.8	700	123	0.64	0.050
T3F100	4.8	831	185	0.71	0.076

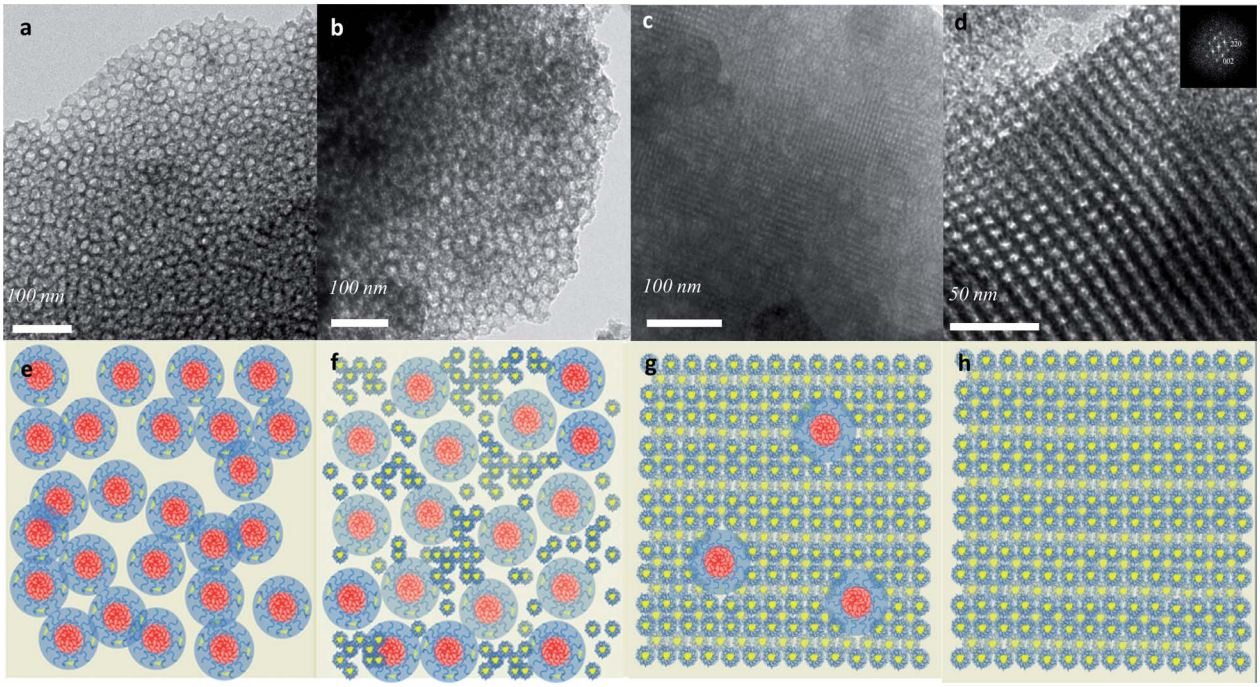

Fig. 2 (a–d) TEM images of (a) T3F0EL100, (b) T3F70EL30, (c) T3F80EL20, and (d) T3F100EL0; (e–h) corresponding correlated illustrative sketches.

random small spheres alternated with large spheres. The SAXS patterns indicate that the intensity of the first peak, belonging to PEO-*b*-PCL at a value of q of 0.24 nm^{-1}, increased upon increasing the PEO-*b*-PCL content; in addition, this signal become sharper and shifted to higher values of q, indicating a well-organized mesoporous structure templated from PEO-*b*-PCL. The decrease in the inter-distance between the larger spherical mesopores was due to the decrease in the F127 content when we increased the PEO-*b*-PCL content in this case. In addition, the intensity of the first peak belonging to F127, at a value of q of 0.58 nm^{-1}, decreased upon increasing the PEO-*b*-PCL content, as would be expected. All of the mesoporous silica samples we prepared at a fixed TEOS-to-F127 ratio of 3 : 0.75 with various PEO-*b*-PCL contents displayed typical type-IV isotherms in their N_2 adsorption/desorption curves [Fig. 3(c)], with two hysteresis loops in the relative pressure (P/P_0) ranges 0.45–0.75 and 0.75–0.95. The pore size distributions of these mesoporous silica samples [Fig. 3(d)], determined on the basis of the BdB model, tended to increase upon increasing the content of PEO-*b*-PCL.

Fig. 4(a) and (b) display TEM images and SAXS patterns, respectively, of the hierarchical mesoporous silica samples we prepared at a fixed TEOS-to-F127 ratio of 3 : 0.9 with various PEO-*b*-PCL contents. Similar to the samples prepared using a TEOS-to-F127 ratio of 3 : 0.75, the intensity of first peak belonging to PEO-*b*-PCL, at a value of q of 0.18 nm^{-1}, increased and the first peak representing F127, at a value of q of 0.58 nm^{-1}, decreased upon increasing the PEO-*b*-PCL content [Fig. 4(b)]. In addition, the patterns became sharper and shifted to higher values of q, indicating well-organized mesoporous structures templated by PEO-*b*-PCL. Whereas we observed only random small spheres alternating with large spheres when we fixed the TEOS-to-F127 ratio at 3 : 0.75 [Fig. 3(a)], the TEM images in Fig. 4(a) reveal a transition from a BCC structure [Fig. 4(a)-(i)] for T3F90EL10 to a structure of random small spheres alternating with large spheres [Fig. 4(a)-(ii)] for T3F90EL30. Further increasing PEO-*b*-PCL content to T3F90EL50, we observed that some of the larger spheres at the sample edge belonging to PEO-*b*-PCL had already transformed into cylinders [Fig. 4(a)-(iii)]. Finally, the TEM images [Fig. 4(a)-(iv)] of T3F90EL70, which featured the highest PEO-*b*-PCL content, were significantly different from those obtained at the other ratios. This sample possessed long-range order in the packing of its small spheres in addition to long-range order of its long-cylinder wall. To further examine its structure, we subjected this sample to microtome cutting and then recorded TEM images (Fig. 5).

Fig. 5(a) presents a top view of the hierarchical mesoporous structure of T3F90EL70; Fig. 5(b) provides a more-detailed view of the circled region, revealing the bimodal mesoporous structure comprising small spherical pores (*ca.* 5.6 nm) and large tetragonal cylinders (diameter: *ca.* 24.5 nm); Fig. 5(c) displays a corresponding correlated illustrative sketch. From Fig. 5(d) and (e), side views of the hierarchical mesoporous structure, we find that the small spheres adhered to the long cylinders of the wall in an orderly manner. Hence, we define this hierarchical mesoporous structure as a "regular spherical strip arrangement alternating with tetragonal cylinders"; Fig. 5(f) presents a corresponding correlated illustrative sketch. We also used FE-SEM to examine this new and unusual hierarchical mesoporous silica structure. Fig. 6(a) provides an enlarged FE-SEM image of T3F90EL70; we observe many 5 nm pores (red arrow) co-existing

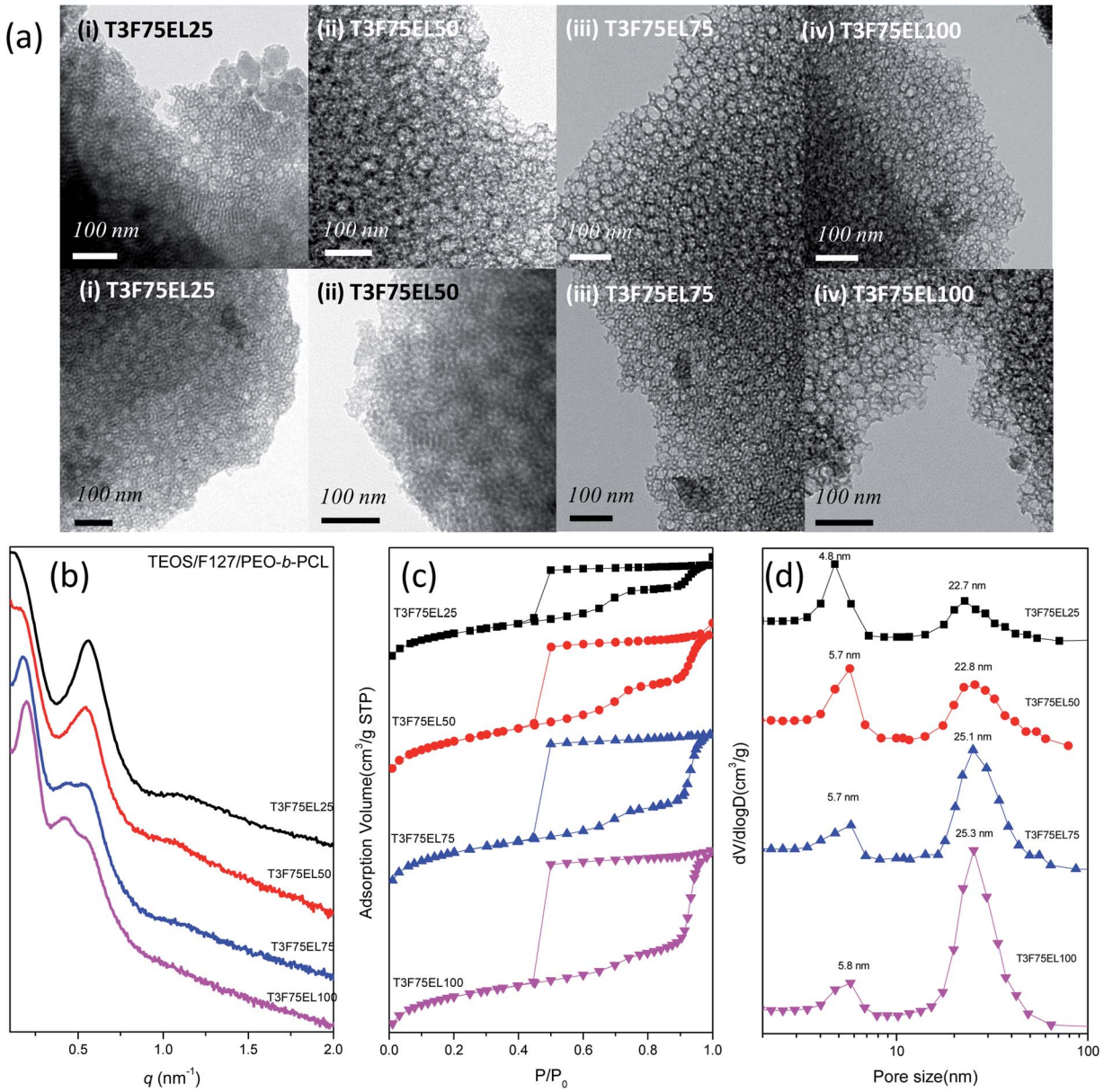

Fig. 3 (a) TEM images, (b) SAXS patterns, (c) N_2 adsorption/desorption isotherms, and (d) pore size distribution curves of hierarchical mesoporous silicas prepared at a fixed TEOS-to-F127 ratio of 3 : 0.75 and various PEO-*b*-PCL weight fractions.

with the 20 nm pores evident in Fig. 6(b). Thus, we could confirm that the mesoporous structures transformed from a regular BCC structure, to random small spheres alternating with large spheres, and finally to a regular spherical strip arrangement alternating with tetragonal cylinders upon increasing the PEO-*b*-PCL content when we fixed the TEOS-to-F127 ratio at 3 : 0.9. The N_2 sorption isotherms of the mesoporous silica samples exhibited [Fig. 4(c)] representative type-IV curves with two sharp capillary condensation steps in the relative pressure ranges from 0.7 to 0.80 and from 0.90 to 1, indicating multimodal pore size distributions. The two hysteresis loops of the T3F90 series are roughly defined, with H_2-like hysteresis loops in the relative pressure (P/P_0) range between 0.45 and 0.7 and other H_2-like hysteresis loops in the range 0.80–0.97, originating from smaller spherical mesopores (F127) and larger spherical or cylindrical mesopores (PEO-*b*-PCL), respectively. Based on the BdB model [Fig. 4(d)], these mesoporous silica samples possess bimodal characteristics: a combination of smaller spherical mesopores (4.7–5.7 nm) and larger spherical or cylindrical mesopores (22.5–25.3 nm). Table 2 provides further details of the textures of these hierarchical mesoporous materials. We also observed that T3F90EL70 had the highest BET surface area because of its unique hierarchical mesostructure: a regular spherical strip arrangement alternating with tetragonal cylinders.

The strengths of the interactions of PEO, PPO, and PCL segments with the OH groups of the silica matrix during a sol–gel reaction follow the order OH/PEO > OH/PPO > OH/PCL.[27] In

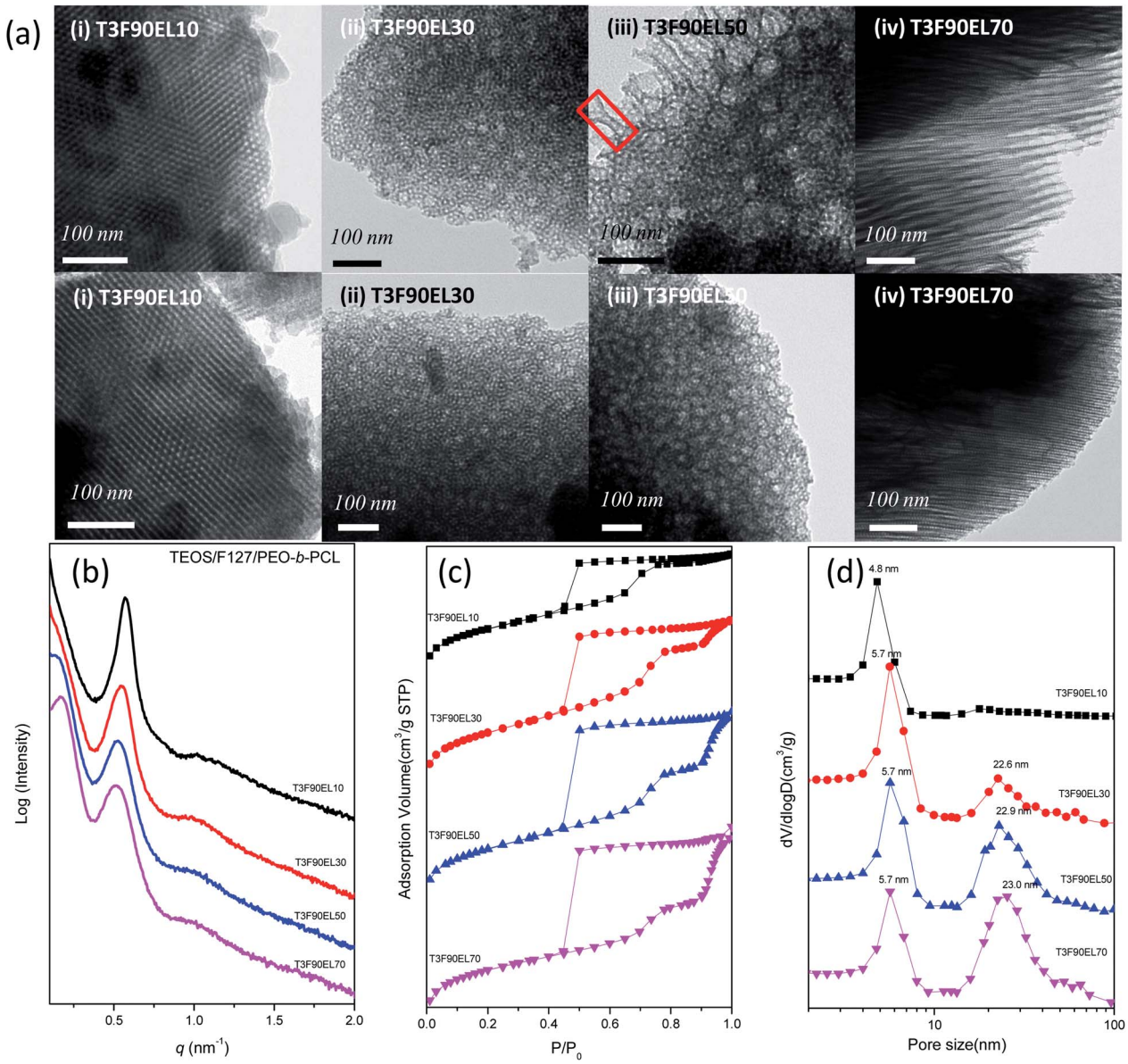

Fig. 4 (a) TEM images, (b) SAXS patterns, (c) N_2 adsorption/desorption isotherms, and (d) pore size distribution curves of hierarchical mesoporous silicas prepared at a fixed TEOS-to-F127 ratio of 3 : 0.9 and various PEO-*b*-PCL weight fractions.

addition, the ether groups of PEO and PPO segments can enter the silica matrix, whereas the C=O groups of PCL segments cannot. As a result, the TEOS/PEO, TEOS/F127, and TEOS/PEO-*b*-PCL ratios are the key factors affecting the competing interactions of the PEO ether, PPO ether, and PCL C=O groups with the OH groups of the silica matrix, thereby influencing the hierarchical mesoporous structures formed when using both F127 and PEO-*b*-PCL as templates. In Table 1, when we fixed the ratio of TEOS to the co-templates (3 : 1), a higher PEO-*b*-PCL/F127 ratio provided a higher TEOS/PPO segment ratio, resulting in smaller spherical pores from the F127 template. For example, we did not observe the mesoporous structure for T3F30EL70, but T3F50EL50 (4.0 nm) and T3F70EL30 (4.8 nm) did feature small mesopores. Similarly, the pore size was approximately 20.2 nm when we used PEO-*b*-PCL as a single template; when we increased the F127 content, the majority of interactions between the OH groups of the silica matrix and the ether groups of PEO-*b*-PCL shifted to become interactions with the ether groups of F127. As a result, the mesoporous size from the PEO-*b*-PCL template generally increased upon increasing the F127 content. For example, the pore sizes were approximately 22.6 and 22.9 nm for T3F30EL70 and T3F70EL30, respectively. Similarly, when we increased the PEO-*b*-PCL contents at fixed TEOS-to-F127 ratios, Table 2 reveals that some of the OH groups of the silica matrix preferred to interact with the ether groups of PEO-*b*-PCL and, thus, the pore size increased from 4.8 nm (T3F75EL25) to 5.7 nm (T3F75EL100) for the F127 template and from 22.7 nm (T3F75EL25) to 25.3 nm (T3F75EL100) for the PEO-*b*-PCL template. Table 2 reveals similar results for the T3F90 samples upon increasing the PEO-*b*-PCL contents.

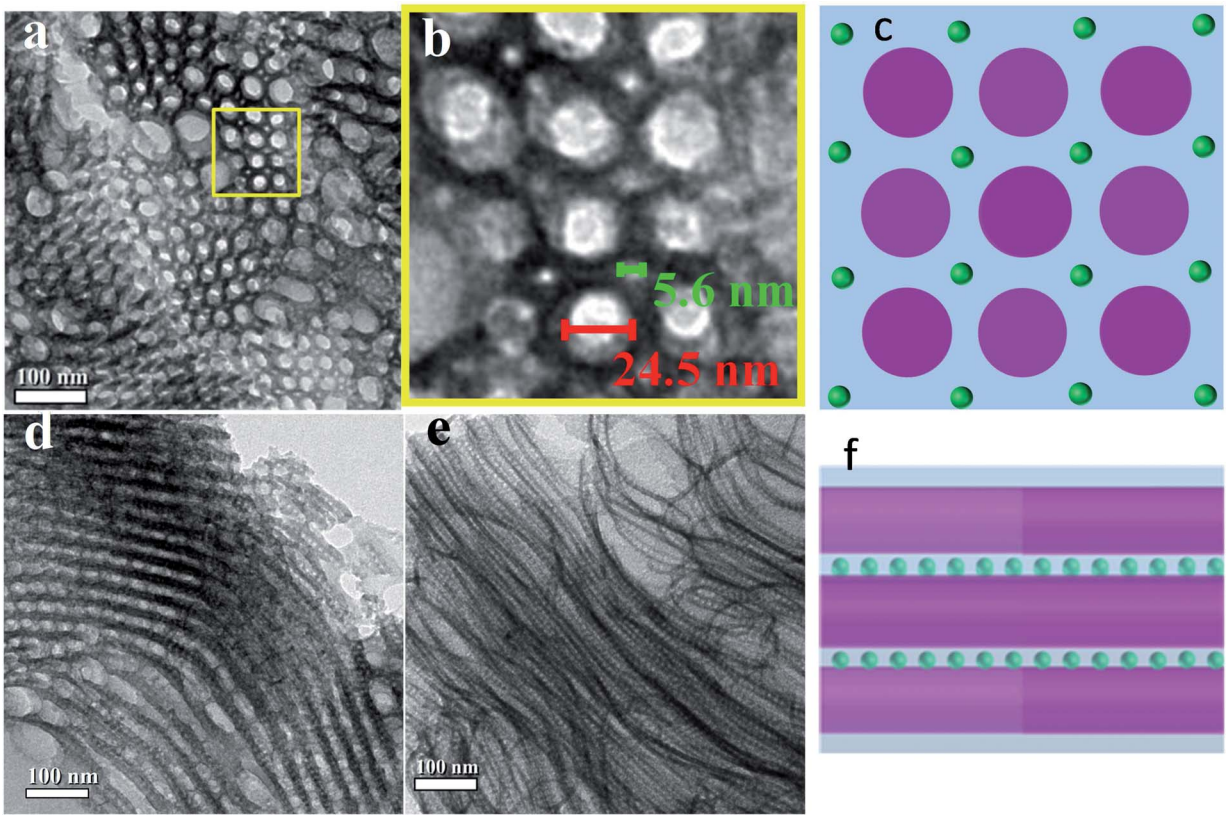

Fig. 5 (a and b) Top and (d and e) side view cutting images and (c and f) correlated illustrative sketches of the mesoporous silica sample T3F90EL70.

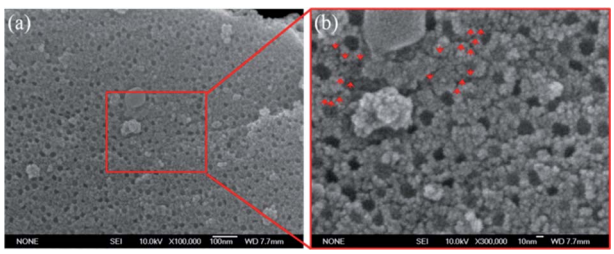

Fig. 6 FE-SEM images of the hierarchical mesoporous silica sample T3F90E70.

Using hierarchical mesoporous structures to fabricate materials with ultra-low refractive indices

Amorphous silica samples synthesized through sol–gel processing typically exhibit high surface areas, microporous structures, high pore volumes, and low refractive indices. For practical applications, it must be possible to prepare thin film samples with high porosity over large areas. In this study, we used a simple spin-coating process to achieve uniform thin film samples; our single-layer antireflection coatings based on mesoporous silicas were capable of decreasing the reflective index from that of glass to 1.08. All the goodness of fit of our samples is above 0.99. The "n&k method" provides a highly accurate and easy to use approach to characterize most thin film

Table 2 Textural properties of mesoporous silica samples prepared at fixed TEOS-to-F127 ratios (3 : 0.75 and 3 : 0.9) and various PEO-*b*-PCL contents

Sample	Pore size (nm)	S_{BET} ($m^2\ g^{-1}$)	S_M ($m^2\ g^{-1}$)	Pore volume ($cm^3\ g^{-1}$)	Micropore volume ($cm^3\ g^{-1}$)
T3F75EL25	4.8; 22.7	624	175	0.63	0.076
T3F75EL50	5.7; 22.8	688	126	0.85	0.051
T3F75EL75	5.7; 25.1	759	225	0.88	0.096
T3F75EL100	5.8; 25.3	722	176	0.99	0.075
T3F90EL10	4.8	700	123	0.64	0.050
T3F90EL30	5.7; 22.6	764	94	0.84	0.035
T3F90EL50	5.7; 22.9	758	107	0.95	0.041
T3F90EL70	5.7; 23.0	781	175	0.99	0.073

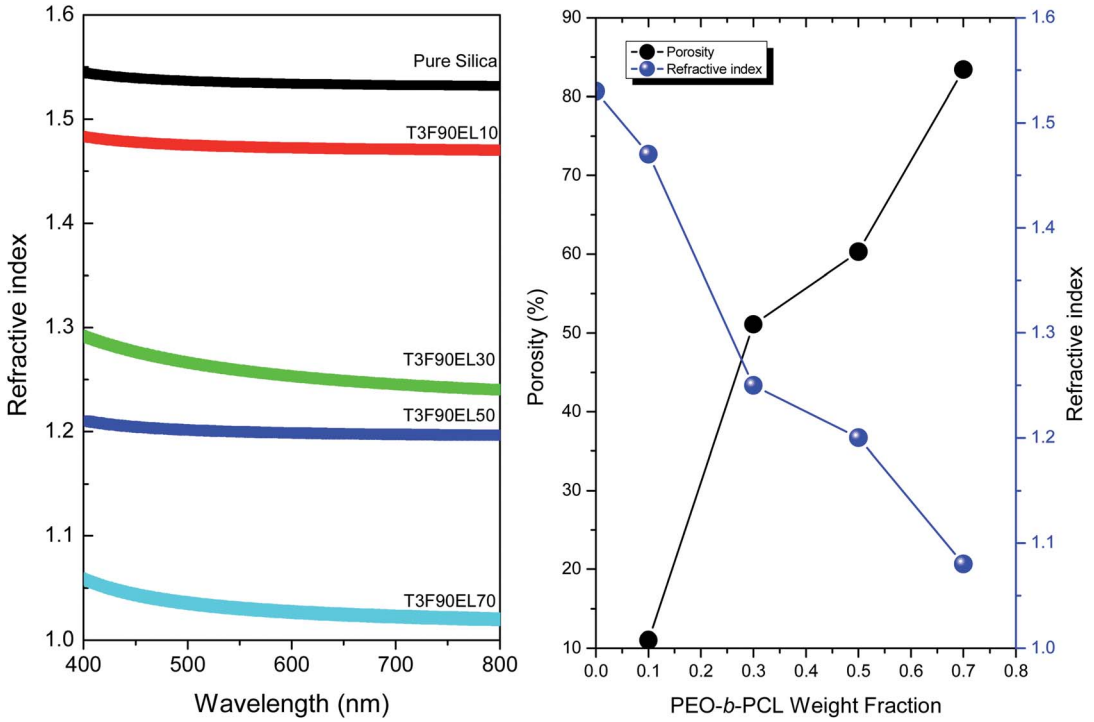

Fig. 7 (a) Refractive indices of pure silica and T3F90 mesoporous silica and (b) the refractive indices and the corresponding porosities of thin films of T3F90 prepared at various weight fractions of PEO-*b*-PCL.

structures of technological importance. Fig. 7(b) displays the porosities and refractive indices at 633 nm of the T3F90 series. We calculated the porosity from the Bruggemann effective medium approximation, given below.[34]

$$f\frac{{n_1}^2-{n_{\text{eff}}}^2}{{n_1}^2+2{n_{\text{eff}}}^2}+(1-f)\frac{{n_2}^2-{n_{\text{eff}}}^2}{{n_2}^2+2{n_{\text{eff}}}^2}=0$$

where n_1 and n_2 are the refractive indices of air and silica, respectively, and f is the volume fraction of air voids in the mesoporous silica. In this study, we used values of n_1 and n_2 of 1.0 and 1.53, respectively (the latter being the refractive index of the silicas synthesized through sol–gel processing, as measured in this study). Although the spin-coating process resulted in more cracks than those formed in the EISA process, some large (*ca.* 20 nm) and small (*ca.* 5 nm) pores were evident on the sample surface (Fig. S2†). Spin-coating is better than EISA processing with respect to both the transmission and mechanical properties of the resulting thin film samples. Fig. 7(a) reveals that the refractive indices (at wavelengths of 400–800 nm) decreased upon increasing the PEO-*b*-PCL content. The wavelengths at which we observed low refractive indices extended to all wavelengths (above 400 nm). Fig. S3† provides refractive indices and extinction coefficient at wavelengths of 200–1000 nm. The rise of the signal below 400 nm is the standard spectral behavior for an absorbing material. Indeed, the shape of real and imaginary part as well as the spectral position of peaks and minima (for real part only) are those expected.[35] Fig. 7(b) reveals that the refractive indices of the films decreased upon increasing the PEO-*b*-PCL content as a result of greater porosities, consistent with the BET surface areas. The refractive indices varied from 1.53 to 1.08 upon adjusting the ratio of TEOS to the co-templates, corresponding to porosities ranging from 11.0 to 83.4% (as determined using the Bruggemann effective medium approximation). Thus, our co-template method allowed the formation of a mesoporous silica having an ultra-low refractive index ($n = 1.08$).

Conclusion

We have developed an excellent co-templating strategy—employing both PEO-*b*-PCL (larger mesopores) and F127 (smaller mesopores) as structure-directing agents—for the fabrication of a series of hierarchical mesoporous silica samples. TEM images and SAXS patterns revealed mesophase transformations of the mesoporous silica samples upon changing the ratios of the PEO-*b*-PCL and F127 block copolymers. The hierarchical mesoporous samples possessing bimodal pore size distributions exhibited high BET surface areas (*ca.* 781 $m^2\ g^{-1}$) and large pore volumes (*ca.* 0.99 $cm^3\ g^{-1}$), as determined through N_2 isotherm sorption experiments, suggesting potential applications as material having ultra-low refractive indices ($n = 1.08$).

Acknowledgements

This study was supported financially by the National Science Council, Taiwan, Republic of China, under contracts NSC 100-2221-E-110-029-MY3 and NSC 100-2628-E-110-001.

References

1 (*a*) H. Chen, J. Wydra, X. Zhang, P. S. Lee, Z. Wang, W. Fan and M. Tsapatsis, *J. Am. Chem. Soc.*, 2011, **133**, 12390–12393; (*b*) K. Moller and M. Bein, *Science*, 2011, **333**, 297–298; (*c*) S. S. Gao, L. Fang, Z. Y. Zhao, Y. Ge, S. Piletsky and A. P. F. Turner, *Adv. Funct. Mater.*, 2013, **23**, 2162–2167; (*d*) K. Ariga, A. Vinu, T. Yamauchi, Q. Ji and J. P. Hill, *Bull. Chem. Soc. Jpn.*, 2012, **1**, 1–32.

2 (*a*) M. Hartmann, *Chem. Mater.*, 2005, **17**, 4577–4593; (*b*) D. J. Wang, Y. Z. Zhen, G. L. Xue, F. Fu, X. M. Liu and D. S. Li, *J. Mater. Chem. C*, 2013, **1**, 4153–4162.

3 J. W. Zhao, F. Gao, Y. L. Fu, W. Jin, P. Y. Yang and D. Y. Zhao, *Chem. Commun.*, 2002, 752–753.

4 (*a*) A. Corma, *Chem. Rev.*, 1997, **97**, 2373; (*b*) Y. Wan and D. Y. Zhao, *Chem. Rev.*, 2007, **107**, 2821–2860; (*c*) Y. S. Hu, P. Adelhelm, B. M. Smarsly, S. Hore, M. Antonietti and J. Maier, *Adv. Funct. Mater.*, 2007, **17**, 1873–1878.

5 C. Y. Lai, B. G. Trewyn, D. M. Jeftinija, K. Jeftinija, S. Xu, S. Jeftinija and V. S. Y. Lin, *J. Am. Chem. Soc.*, 2003, **125**, 4451–4459.

6 J. Moghal, J. Kobler, J. Sauer, J. Best, M. Gardener, A. A. R. Watt and G. Wakefield, *ACS Appl. Mater. Interfaces*, 2012, **4**, 854–859.

7 (*a*) J. Rodriquez-Hernandex, F. Checot, Y. Gnanou and S. Lecommandoux, *Prog. Polym. Sci.*, 2005, **30**, 691–724; (*b*) R. Markus and J. Ulrich, *Adv. Funct. Mater.*, 2013, **23**, 5381–5389; (*c*) J. Wei, Q. Yeu, Z. Sun, Y. Deng and D. Y. Zhao, *Angew. Chem., Int. Ed.*, 2012, **51**, 6149–6153; (*d*) Y. Li, A. Keilbach, N. Mizoshita, S. Inagaki and T. Bein, *J. Mater. Chem. C*, 2014, **2**, 50–55.

8 (*a*) J. G. Li, R. B. Lin and S. W. Kuo, *Macromol. Rapid Commun.*, 2012, **33**, 678–682; (*b*) J. G. Li, R. B. Lin and S. W. Kuo, *RSC Adv.*, 2013, **3**, 17411–17423.

9 (*a*) W. C. Chen, S. W. Kuo and F. C. Chang, *Polymer*, 2010, **51**, 4176–4184; (*b*) S. W. Kuo, *Polymer. Int.*, 2009, **58**, 455–464.

10 (*a*) L. Y. Shi, Y. Zhou, Z. Shen and X. H. Fan, *Macromolecules*, 2012, **45**, 5530–5537; (*b*) A. Dehghan and A. C. Shi, *Macromolecules*, 2013, **46**, 5796–5805.

11 G. Riess, *Prog. Polym. Sci.*, 2003, **28**, 1107–1170.

12 W. H. Southwell, *Opt. Lett.*, 1983, **8**, 584–586.

13 J. A. Dobrowolski, D. Poitras, P. Ma, H. Vakil and M. Acree, *Appl. Opt.*, 2002, **41**, 3075–3083.

14 R. Badugu, E. Descrovi and J. R. Lakowicz, *Anal. Biochem.*, 2014, **445**, 1–13.

15 J.-Q. Xi, M. Ojha, J. L. Plawsky, W. N. Gill, J. K. Kim and E. F. Schubert, *Appl. Phys. Lett.*, 2005, **87**, 031111.

16 J.-Q. Xi, M. Ojha, W. Cho, J. L. Plawsky, W. N. Gill, T. Gessmann and E. F. Schubert, *Opt. Lett.*, 2005, **30**, 1518–1520.

17 G. Canazza, F. Scotognella, G. Lanzani, S. De Silvestri, M. Zavelani-Rossi and D. Comoretto, *Laser Phys. Lett.*, 2014, **11**, 035804.

18 J. H. Lee, C. Y. Koh, J. P. Singer, S. J. Jeon, M. Maldovan, O. Stein and E. L. Thomas, *Adv. Mater.*, 2014, **26**, 532–569.

19 H. A. Macleod, *Thin Film Optical Filters*, Institute of Physics Pub, Bristol and Philadelphia, 2001, vol. 3.

20 Y. Kanamori, M. Sasaki and K. Hane, *Opt. Lett.*, 1999, **24**, 1422–1424.

21 M. Ibn-Elhaj and M. Schadt, *Nature*, 2001, **410**, 796–799.

22 T. Glaser, A. Ihring, W. Morgenroth, N. Seifert, S. Schroter and V. Baier, *Microsyst. Technol.*, 2005, **11**, 86–90.

23 Z. Wu, J. Walish, A. Note, L. Zhai, R. E. Cohen and M. F. Rubner, *Adv. Mater.*, 2006, **18**, 2699–2702.

24 B. G. Prevo, Y. Hwang and O. D. Velev, *Chem. Mater.*, 2005, **17**, 3642–3651.

25 H. Y. Hsueh, H. Y. Chen, M. S. She, C. K. Chen, R. M. Ho, S. Gwo, H. Hasagawa and E. L. Thomas, *Nano Lett.*, 2010, **10**, 4994–5000.

26 M. Ruetschi, P. Grutter, J. Funfschilling and H. J. Guntherodt, *Science*, 1994, **265**, 512–514.

27 L. Innocenzi, L. Malfatti and G. Soler-Illia, *Chem. Mater.*, 2011, **23**, 2501–2509.

28 (*a*) J. G. Li and S. W. Kuo, *RSC Adv.*, 2011, **1**, 1822–1833; (*b*) J. G. Li, Y. D. Lin and S. W. Kuo, *Macromolecules*, 2011, **44**, 9295–9309; (*c*) J. G. Li, Y. H. Chang, Y. S. Lin and S. W. Kuo, *RSC Adv.*, 2012, **2**, 12973–12982; (*d*) J. G. Li, C. Y. Chuang and S. W. Kuo, *J. Mater. Chem.*, 2012, **22**, 18583–18595.

29 A. R. Forouhi and I. Bloomer, *Phys. Rev. B: Condens. Matter Mater. Phys.*, 1986, **34**, 7081.

30 A. R. Forouhi and I. Bloomer, *Phys. Rev. B: Condens. Matter Mater. Phys.*, 1988, **38**, 1865–1874.

31 A. R. Forouhi and I. Bloomer, 1990, U.S. Patent No. 4,905,170.

32 W. C. Chu, S. F. Chiang, J. G. Li and S. W. Kuo, *RSC Adv.*, 2014, **4**, 784–893.

33 Y. K. Jung, M. H. Park, H. J. Moon, U. P. Shinde and B. Jeong, *Macromolecules*, 2013, **46**, 4215–4222.

34 (*a*) D. E. Aspnes, *Thin Solid Films*, 1982, **89**, 249; (*b*) H. Y. Chen, H. W. Lin, C. Y. Wu, W. C. Chen, J. S. Chen and S. Gwo, *Opt. Express*, 2008, **16**, 8106–8116.

35 F. Wooten, *Optical Properties of Solids*, Academic Press, New York and London, 1972.

